

Multi-Disciplinary Multi-Point Robust Design Optimization of a Turbocharger Impeller

Athanasiou Poulos^{1*}, Remy Nigro², Dirk Wunsch¹, Charles Hirsch¹

¹ Numeca International, Chaussée de la Hulpe, 189, 1170 Brussels, Belgium

² University of Mons, Fluids-Machines Department, Mons, Belgium

Email: athanasiou.poulos@numeca.be, remy.nigro@umons.ac.be, dirk.wunsch@numeca.be, charles.hirsch@numeca.be

Summary

A recently developed strategy for Robust Design Optimization (RDO), i.e. optimization under uncertainties while reducing the variability of the system output with respect to the input uncertainties is applied to a turbocharger impeller. The RDO strategy relies on the non-intrusive probabilistic collocation method for the propagation of uncertainties and a global surrogate assisted optimization strategy, where a mixed Design of Experiments (DoE) is built. This mixed DoE comprises both design variables and uncertainties as individual dimensions. A recent application of this RDO strategy to an axial compressor blade showed that a multi-point formulation is of foremost importance for an industrial application of robust design optimization, since otherwise off-design points become less robust. The turbocharger impeller was studied in a previous work using a deterministic multi-disciplinary multi-point strategy. In the current work a robust design optimization formulation is set-up and applied to the turbocharger impeller. Given that the investigated turbocharger compressor has an active self-recirculation casing treatment design, the multi-point optimization problem combines three operating points on two different speed lines: One operating point close to choke and one close to stall conditions on the higher speed line and one operating point close to stall conditions on the lower speed line. The multi-disciplinary formulation comes from the calculation of mechanical stresses of the various designs. The importance and benefits of the robust design optimization formulation are shown in comparison with the deterministic optimization of the same geometry.

Keywords: optimization under uncertainty, uncertainty quantification, robust design optimization, automotive centrifugal compressor.

1 Introduction

The design of turbomachinery blades is a highly complex and multidisciplinary task. Automotive turbochargers for example face the challenge of heavy exhaust gas recirculation, which is needed to meet stringent emission regulations and to reach fuel efficient engines. These challenges are addressed nowadays by means of virtual prototyping. This involves various disciplines such as Computational Fluid Dynamics (CFD) or Computational Structural Mechanics (CSM). However, the design process is still overwhelmingly deterministic, neglecting the influences of uncertainties. At the same time uncertainties resulting from manufacturing or assembly variability or varying operating conditions can have a significant influences on the performance stability. It is thus the goal of robust design optimization to aim at an improved performance but at the same time to guarantee a stable performance if the geometry deviates from the design geometry or operating conditions deviate from the nominal flow conditions. These aspects need to be included in the future design process in order to provide a range of confidence with the simulation results. In this work, such a robust design optimization is applied to an automotive turbocharger, which relies on exhaust gas recirculation.

2 Optimization framework

Numeca's FINE™/Design3D optimization framework is used in conjunction with the FINE™ tool chain from meshing

(AutoGrid5™), parametric modelling (AutoBlade™), and flow solver (FINE™/Turbo). In the following the general principle of the deterministic optimization chain as well as its individual components are described.

2.1. General principle

The general principle of FINE™/Design3D relies on four main building blocks. First, a parametric modeler that allows to re-engineer turbomachinery geometries and consequently modify the geometries by changing the values of the design parameters used. In this work the in-house AutoBlade™ modeler is used, but any external modeler can be coupled into the optimization chain. Based on the parametric model a Design of Experiment (DoE) is built with the goal to sample the n -dimensional design space, where n is the number of design variables. Each sample in the DoE represents a full 3D CFD-CSM simulation. These samples are used to build an approximate solution, a so-called surrogate model, spanning over the entire design space by “interpolating” the system response between the sample points. This allows to perform the optimization on the surrogate model instead of having to run full 3D CFD-CSM simulations for every optimization sample. The optimization strategy is global in the sense that the optimizer searches for an optimal configuration everywhere in the design space. To this end a Genetic Algorithm is used, which is inspired by the evolutionary selection process in nature. The objective and constraint formulation can be either single objective, where several objectives and constraints are represented by a weighted sum or multi-objective, where the

optimal designs are found on a so-called Pareto Frontier. All designs on the m -dimensional Pareto Frontier are non-dominated by any other design, i.e. they are the best samples for the given n -dimensional combination of objectives.

2.2. Parametric modeller

AutoBlade™ is a parametric modeler particularly suited for the representation of turbomachinery configurations. The blades are fitted by two-dimensional approximations in several spanwise sections of the blade. These sections are then stacked to rebuild the 3D blade geometry. Two design modes are available for the construction of the blade sections. The first, which is often used for turbine blades, constructs the blade sections with independent pressure and suction sides. The second, which is used here and is more suited for centrifugal designs, is based on the definition of the camber line and an addition of a thickness distribution in order to build pressure and suction sides. The endwalls are also parameterized and all curves are generally represented by Bezier-Curves.

2.3. Design of Experiment

Based on the parametric representation of the geometry a subset of parameters is selected for design optimization. This means that the selected parameters are allowed to vary within pre-defined bounds. In order to cover the design space in a computationally efficient way, different types of Design of Experiment exist, such as Latin Hypercube Sampling, which is used in this work.

2.4. Surrogate model

Performing design optimization on engineering relevant 3D designs including CFD and CSM is computationally expensive. In order to accelerate the optimization process an approximation of the system response is built based on the DoE samples. The surrogate model (or response surface model) can be thought of as a multi-dimensional interpolation of the design space, which allows to predict the system output (i.e. the computed quantities like efficiency, mass flow, etc.) in between the sample points of the DoE.

2.5. Optimization algorithm

Based on the surrogate model the optimization algorithm, which is a global search genetic algorithm performs hundreds of system evaluations at a much reduced cost. This procedure would computationally not be feasible without the surrogate model. The optimizer used is a Genetic Algorithm inspired by the evolutionary selection process in nature and works with generations. Every subsequent generation inherits from the previous generation through different mechanisms. First, elitism allows to keep the best samples in the next generation. Additional new samples are built based on combinations of several members of the previous generation and by mutation, where random effects are introduced. Every next generation performs better in terms of the defined objectives than the previous generation. Eventually, after the completion of one optimization cycle, which consists of several or even hundreds of generations on the surrogate, one or several best designs are retained and run as 3D CFD-CSM simulations. The surrogate

is consequently re-calculated and its quality is improved around the optimal solutions calculated by 3D simulations.

2.6. Objective functions and constraints

There are two possibilities of defining a multi-objective design optimization problem. First, all the objectives and constraints can be summarized into a weighted sum of objectives and constraints. In such a way that the multi-objective optimization problem is reformulated into a single objective problem. In this case the optimum depends on the *a priori* selection of the weights chosen. The second possibility is a true multi-objective formulation and as consequence there is not one single optimum solution, but rather an ensemble of optimal solutions, which are referred to as Pareto Frontier. This Pareto Frontier contains the non-dominated samples, which means that no other sample is performing better at this specific point in the multi-dimensional response space. Using this formulation the selection of the optimal design is performed after the optimization process, where the design engineer needs to weigh different and often contradicting objectives. A multi-objective formulation is used in this work.

2.7. Multipoint optimization

Industrial relevant designs need very often not only to be optimized at their design point, but need also to perform well in off-design configurations. As an example, increasing the stall margin could be one of the objectives. The optimization framework allows to perform multi-point optimization, where the operational points lie on different speed lines. This is used in the present work.

3 Uncertainty Quantification (UQ) method

The uncertainty propagation method used within this work is the non-intrusive probabilistic collocation method [5]. It is based on the expansion of the solution into Lagrange interpolating polynomials. The basis points of the polynomial expansion (the collocation points) are chosen as the as the Gauss quadrature points by means of the Golub-Welsh algorithm for general Probability Density Function shapes [2]. A system of uncoupled simulations can be derived, which has the advantage that this UQ propagation technique can be wrapped around the flow solver in a non-intrusive way.

3.1. Statistical output moments

Based on the output of the performed simulations, statistical moments of any output quantity ϕ are automatically calculated, by taking the weights w_k from the Gauss quadrature. The mean, variance, skewness and kurtosis are calculated following Eq. (1) and Eq. (2). This information is calculated for a selected number of scalar output quantities as follows:

$$\text{Mean: } \mu_1 = \sum_{k=1}^{N_p} w_k \phi_k(\bar{x}, t) \quad (1)$$

and the second (variance, $n=2$), third (skewness, $n=3$) and fourth moment (kurtosis, $n=4$) are calculated as follows:

$$\mu_n = \sum_{k=1}^{N_p} w_k (\phi_k(\bar{x}, t) - \mu_1)^n \quad (2)$$

3.2. Output PDF reconstruction

Based on the first four statistical output moments, a PDF can be reconstructed. This is important, because the display of non-deterministic results by a mean value with an uncertainty bar corresponding to $\pm\sigma$ implies a symmetric distribution around the mean value, whereas the real system response might be characterized by a skewed distribution. To overcome this, the Pearson method [7] is used to reconstruct an approximation of the PDF of a given output quantity from its first four moments. Figure 1 shows a schematic of the standard PDF shapes to be selected in function of the third and fourth statistical output moment by the Pearson method.

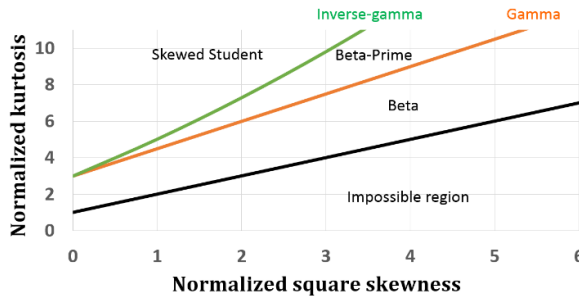


Fig. 1. Schematic of Pearson method.

3.3. Multiple simultaneous uncertainties

Industrial design challenges are usually characterized by a multitude of simultaneous uncertainties, that cannot be considered one-by-one, whether they are correlated or not. Given that quadrature is used to determine the collocation points, the problem of multiple simultaneous uncertainties boils down to a multi-dimensional quadrature problem. The standard approach is a tensor product, which, however, suffers from the “curse of dimensionality”. This means the computational cost increases exponentially with the number of uncertainties considered. In the current work a sparse grid quadrature, based on Smolyak’s quadrature method [8] is used. Table 1 summarizes the number of quadrature points contained in linear growth sparse grid for levels of 1 and 2 in comparison with a full-tensor grid with the same number of 1D quadrature points [10].

Table 1. Number of quadrature points N_p contained in full tensor grid and sparse grid.

Level	1		2		
	Dimension	Tensor	Sparse	Tensor	Sparse
1		3	3	5	5
2		9	5	25	17
3		27	7	125	31
4		81	9	625	49
5		243	11	3125	71
...	
10		59049	21	$\approx 9.7 \times 10^6$	241

The significant reduction in number of runs makes the simultaneous treatment of many uncertainties in complex 3D CFD problems accessible.

3.4. Scaled sensitivity derivatives

An important element in the evaluation of non-deterministic solutions is the relative influence of a given input uncertainty on the solution. This influence is estimated by scaled sensitivity derivatives, as in [9], and applied to the probabilistic collocation method. The scaled sensitivity derivative is defined as the partial derivative of the solution $u(\bar{x}, t, \xi)$ with respect to the uncertain input parameter ξ , multiplied with the standard deviation of the uncertain input parameter as:

$$\sigma_{\xi_i} \frac{\partial u(\bar{x}, t, \xi)}{\partial \xi_i} \quad (3)$$

This provides, on the one hand, the understanding of the system under investigation and a variation of an uncertain input can be directly linked to a variation in the output quantity of interest. On the other hand, it provides an objective measure of the influence of uncertainties on the output and allows therefore for an efficient reduction in number of uncertainties by identifying uncertainties with little influence on the solution.

4 Robust Design Optimization formulation

The optimization objectives and constraints are not single values in robust optimization, but the mean value and standard deviation of the objective functions. These statistical moments, which are the output of the UQ method described above, need to be calculated for every single design optimization. The most straightforward approach would be to run full 3D CFD simulations for every point in the DoE and calculate a surrogate model for the statistical moments. This is, however, very costly, since a database usually contains hundreds of points.

The proposed solution is a mixed Design of Experiment (DoE) comprising of both the design variables and the uncertainties. To build this mixed DoE, the uncertainties are added as additional dimensions to the DoE, which requires harmonizing the way the dimensions are sampled independently from their type of distribution. Generally, design parameters in traditional DoE based optimization are sampled uniformly from a given interval $[a, b]$. If expressed in terms of a PDF, such as depicted in figure 2, sampling is done from a uniform PDF. To combine the sampling of design variables with the sampling of uncertainties, the PDF (uniform) is represented by its Cumulative Distribution Function (CDF), which on its ordinate ranges from 0 to 1. If the ordinate is divided into equal probable sections, the values of the design parameters corresponding to these sections account for the same probability.

For an arbitrary PDF shape, such as sketched in fig. 3, the principle remains the same. The PDF is expressed as CDF and it is divided into equal probable intervals, which are mapped

onto the uncertain parameter. The probability interval spacing (on the ordinate) is uniform in both cases, but the design and uncertain parameter spacing varies in function of the PDF shape. A more detailed description can be found in [3].

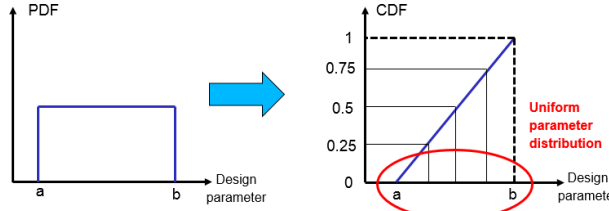


Fig. 2. Sampling of a design parameter from a uniform distribution in interval $[a, b]$. From [3].

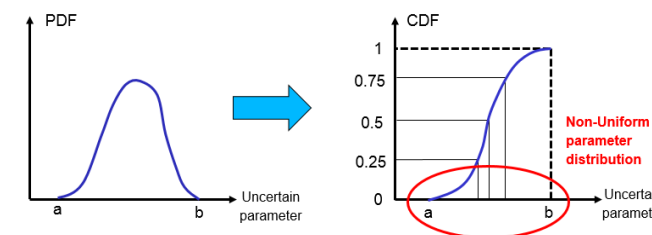


Fig. 3. Sampling of an uncertain variable from an arbitrary probability density function in interval $[a, b]$. From [3].

5 Turbocharger Impeller: Description

The turbocharger compressor studied was numerically and experimentally investigated by FORD Motor Company for a wide operation range. It uses an active self-recirculation casing treatment that extends the compressor flow capacity and improves the surge margin without any efficiency penalty through dual bleed slots [4]. The impeller was already the subject of a multi-point multi-disciplinary optimization study [1], where the deterministic multi-objective optimization problem was expressed as a single objective optimization problem, making use of a weighted sum for the objectives and constraints.

5.1. Geometry and flow conditions

The impeller comprises 6 main and 6 splitter blades and needs to perform over a wide range of rotational speeds. Figure 4 shows the blade geometry.

Figure 5 reprints the result of the optimization [1] for the pressure ratio over non-dimensional mass flow. It illustrates how the variable geometry is used over a wide operation rate for a constant speed line. ‘Position 1’ is used in operating conditions from choke to the design point, while ‘Position 2’ is used from the design point to stall. As a consequence, two different meshes are used for points close to choke and close to stall respectively.

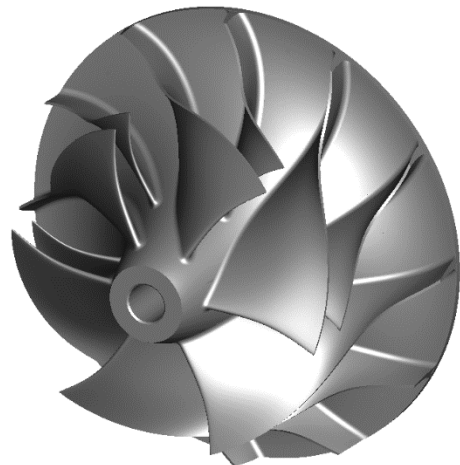


Fig. 4. Solid model of the investigated compressor.

Three different operating points on two different speed lines are used in the present multi-point optimization study:

- Choke conditions, 120,000 rpm
- Stall conditions, 120,000 rpm
- Stall conditions, 40,000 rpm
- Mechanical stresses at 135,000 rpm

Following [1] these operating points are chosen because they are more critical to performance than the design point. It is expected that the design point follows the positive evolution of the extreme conditions. This effect can also be seen in Figure 5.

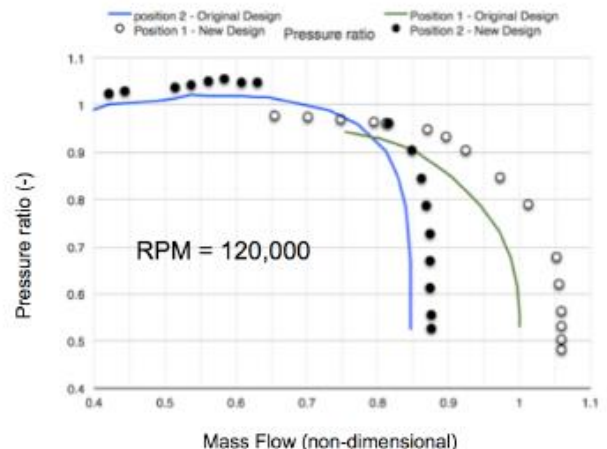


Fig. 5. Pressure ratio over non-dimensional mass flow [1]

5.2. Parametric model

A parametric model consists of a total of 294 parameters which are used to reconstruct the shape of the blades, the endwalls and the solid body model which will be used for the Finite Element Analysis (FEA) to assess the stresses present on the model. Of these parameters, 19 are free to variate for the optimization purposes. In order to ensure that all designs are realistic and can be manufactured, some of the free parameters are dependent on other parameters through mathematical expressions. An extended definition of the parametric model used is given in [1].

5.3. Operational and geometrical uncertainties

The following uncertainties are propagated and taken into account during the robust design optimization.

Geometrical

- Tip gap height $\pm 25\%$ (symmetric beta-PDF)
- Blade thickness $\pm 1\%$ (symmetric beta-PDF)

Operational

The boundary conditions used for the simulations at stall and choke conditions are not the same. While at the stall points, the total pressure is imposed at the inlet, at the choke point the static pressure at the outlet is imposed. The uncertainty imposed is:

- $\pm 1\%$ (symmetric beta-PDF) of the total pressure at the inlet or static pressure at the outlet respectively

6 Deterministic design optimization

The deterministic multi-disciplinary multi-point optimization problem is characterized by its design variables, operating conditions and multi-disciplinary objective and constraint formulations. In view of a comparison with the robust design, it is formulated as a multi-objective optimization problem.

6.1. Design variables

A total of 19 design parameters is used for the description of the optimization problem:

- 2 parameters for the hub line
- 3 parameters for the camber line in two sections, i.e. a total of 6 parameters
- 3 parameters for the camber line of the splitter in two sections, i.e. a total of 6 parameters
- 1 parameter for the meridional location of the splitter
- 2 parameters for the tangential location of the splitter
- 2 parameters for the tangential stacking

The parameters of the camber line definition of the blade sections are optimized, while the thickness distribution is kept constant.

6.2. Operating points

The flow conditions taken into the multi-point optimization are the following:

- Choke conditions for high rotation speed at 120000rpm
- Stall conditions for high rotation speed at 120000rpm
- Stall conditions for low rotation speed at 40000rpm
- Mechanical stresses are calculated at a rotation speed of 135000rpm , which is 5000rpm higher than in [1]

6.3. Deterministic Design: Objective and constraint formulation

The overall objectives and constraints are the following:

- Improve or not deteriorate the performances
- Improve stall margin

- At least keep the capacity (choke mass flow)
- Maintain the peak mechanical stresses

The back plate was optimized with respect to mechanical stresses in [1] and the already optimized geometry is taken for this study. As a consequence a constraint is formulated on the mechanical stresses. This translates into the following objective and constraint formulations:

- Maximize efficiency in the two stall points (2 objectives)
- Maximise choke mass flow (1 objective)
- Maintain level pressure ratio in the two stall points (2 constraints)
- Maintain level of von Mises Stresses (1 constraint)

7 Robust design optimization

The robust design formulation is the following.

7.1. Design variables and uncertainties

The design variables are the same as for the deterministic optimization and listed in section 6.1 and the uncertainties included are the ones listed in section 5.3.

7.2. Operating points

The same operating points as for the deterministic optimization are considered as listed in section 6.2.

7.3. Robust Design: Objective and constraint formulation

The global design objectives remain the same, however, in robust design optimization the uncertainties are taken into account. The optimization is formulated in a robust way with respect to the performances. This translates into the following objective and constraint formulations:

- Maximize the mean value of the efficiency in the two stall points (2 objectives)
- Minimize the standard deviation of the efficiency in the two stall points (2 objectives)
- Maximize the mean value of the choke mass flow (1 objective)
- Minimize the standard deviation of the choke mass flow (1 objective)
- Maintain the level of the mean value of the pressure ratio in the two stall points (2 constraints)
- Maintain the level of the mean value of von Mises Stresses (1 constraint)

8 Analysis of robust design optimization and comparison with deterministic design optimization

As shown in sections 6 and 7, the difference between deterministic and robust design optimization lies mainly in the definition of the optimization objectives. While the deterministic optimization maximizes the efficiency, the robust design optimization maximizes the mean value of the efficiency and simultaneously minimizes the standard deviation of efficiency. Both optimization studies in this work

are based on multi-objective formulations, where the robust design optimization has a higher number of objectives, which are the statistical moments (mean and standard deviation) of the same objective functions as the deterministic optimization. In order to compare deterministic and robust design UQ studies are performed on the found deterministic optimal designs. This allows to plot the deterministic designs in the Pareto diagrams of the robust design optimization, showing the mean value and standard deviation of the quantities of interest.

8.1. Deterministic design optimization

The deterministic design optimization reaches the objectives defined under section 6.3 as shown in the Pareto diagrams in figures 6 to 11. All values are normalized by the value of the original design. Increasing the choke mass flow and improving the peak efficiency near stall are shown to be conflicting objectives since they form a clear Pareto frontier for rotational speeds of 120,000rpm and 40,000rpm respectively (as seen in fig. 6 and fig. 7). The original design proves to be a compromise between peak efficiency near stall and maximum choke mass flow and lies close the Pareto frontier.

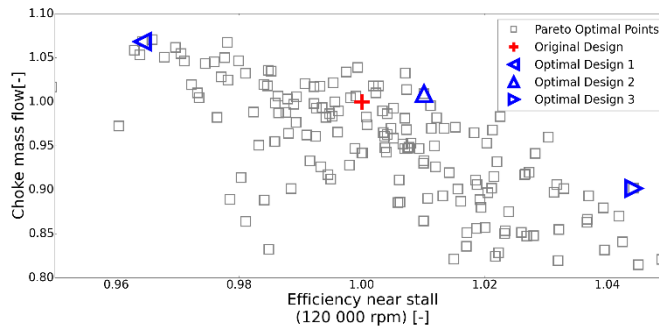


Fig. 6: Pareto plot for choke mass flow over efficiency at 120,000rpm

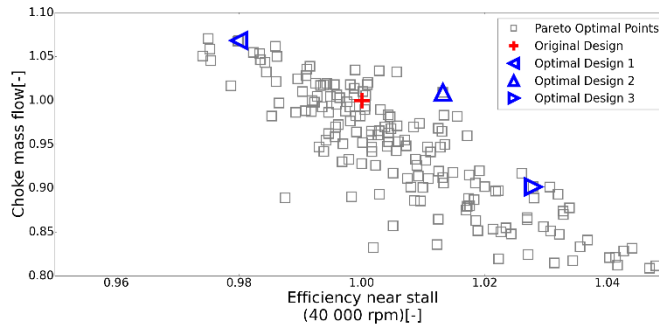


Fig. 7: Pareto plot for choke mass flow over efficiency at 40,000rpm

Three optimal designs are selected, which are discussed in the following. Design 1, which increases the choke mass flow by 6.8%, but reduces the peak efficiency by 3.6%, Design 2, which improves both choke mass flow and peak efficiency near stall by 0.9% and 1.0% respectively, and Design 3, which maximizes peak efficiency near stall by 4.4%, but reduces the choke mass flow by 9.9%. It is shown in fig. 8 to 11 that all

three designs keep the von Mises stresses in an acceptable range and keep nearly constant or increase slightly the pressure ratio for all designs. Only exception is design 3 that shows a slightly reduced pressure ratio at 40,000rpm. All values are listed in table 2.

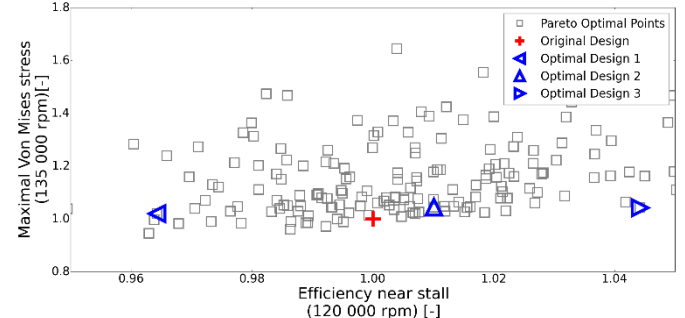


Fig. 8: Pareto plot for von Mises stresses over efficiency at 120,000rpm

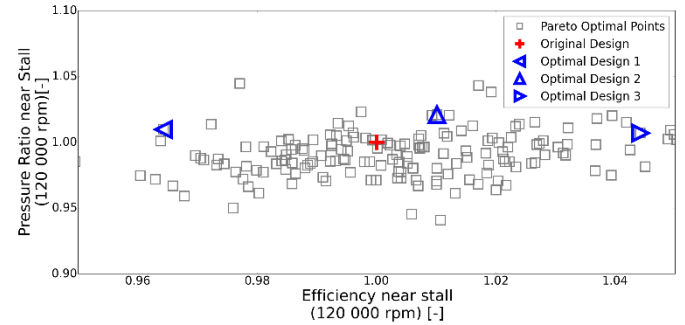


Fig. 9: Pareto plot for pressure ratio over efficiency at 120,000rpm

Given the global objectives as defined deterministic design 2 is the optimal design of choice as it increases both the choke mass flow and efficiency near stall, while keeping the mechanical stress levels under the critical range and slightly improving the pressure ratio.

Table 2. Normalized objective function values of deterministic optimal design.

	η_{120}	η_{40}	m_{choke}	Π_{120}	Π_{40}	$\sigma_{\text{von Mises}}$
Original	1	1	1	1	1	1
Design 1	0.964	0.980	1.068	1.010	1.003	1.020
Design 2	1.010	1.013	1.009	1.021	1.001	1.044
Design 3	1.044	1.028	0.901	1.007	0.999	1.042

Figure 10 shows flow velocity vectors together with the colour contour of the magnitude of the flow velocity for the near stall point at 120,000rpm. A recirculation through the bleed slot is installed at low mass flows. For high mass flow rates close to choke conditions some flow bypasses the first part of the impeller as seen in fig. 11. This increases the range of

operability on the choke side by adding additional mass through the bypass to the impeller and by not limiting it to the choking mass flow rate.

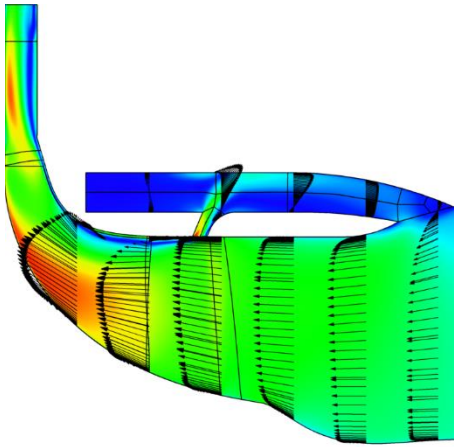


Fig. 10: Original Design: Flow velocity vectors and colour contour of the magnitude of the flow velocity (near stall point at 120,000rpm)

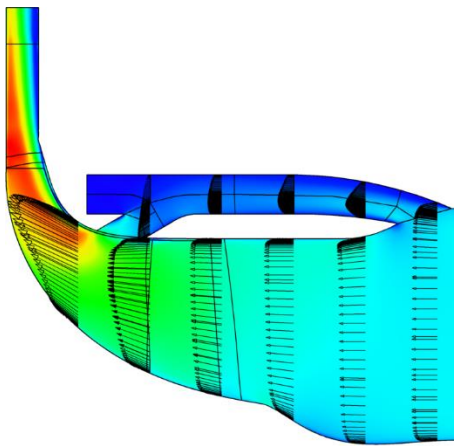


Fig. 11: Original Design: Flow velocity vectors and colour contour of the magnitude of the flow velocity (near choke at 120,000rpm)

Figures 12 and 13 show optimal Design 1 and Design 3 which have the highest and lowest choke mass flow rate of the retained designs, respectively. Figure 12 shows that the flow velocity is significantly increased in the bypass for Design 1 compared with the original design and Design 3. The hub line is a free design parameter for the optimization, which leads to a design that accelerates the flow due to the hub shape as seen in fig. 13 if compared with the original hub design in fig. 11.

To indicate the zones of flow losses across the impeller the entropy is visualized in several streamwise cutting planes from before the leading edge of the impeller, across the blade, shortly after the trailing edge and into the vaneless diffuser. The entropy colour contours are shown in fig. 14 (original design), fig. 15 (design 1) and fig. 16 (design 3) respectively.

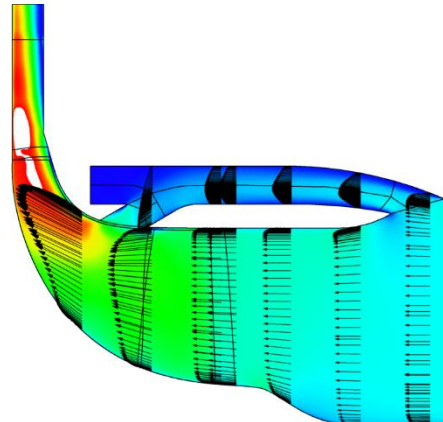


Fig. 12: Design 1: Flow velocity vectors and colour contour of the magnitude of the flow velocity (near choke at 120,000rpm)

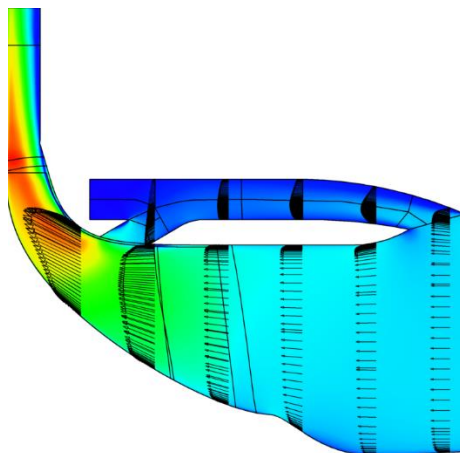


Fig. 13: Design 3: Flow velocity vectors and colour contour of the magnitude of the flow velocity (near choke at 120,000rpm)

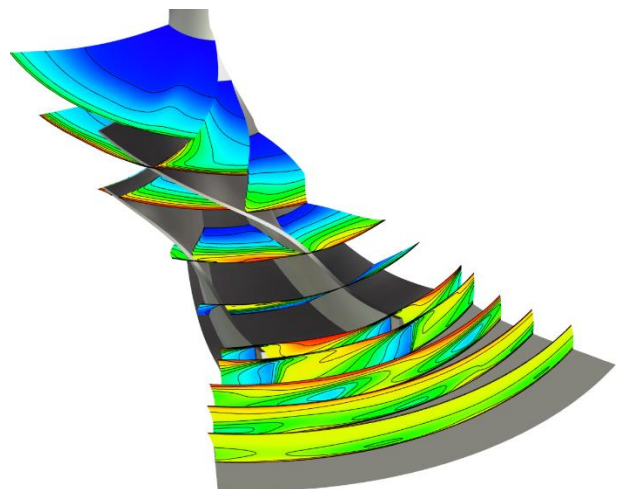


Fig. 14: Original design: Entropy and entropy isolines along streamwise cuts

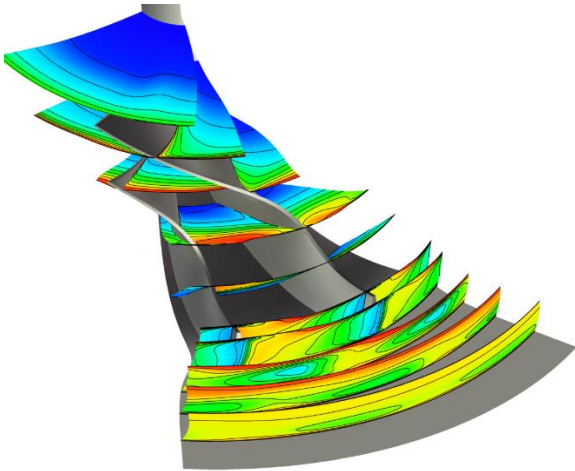


Fig. 15: Design 1: Entropy and entropy isolines along streamwise cuts

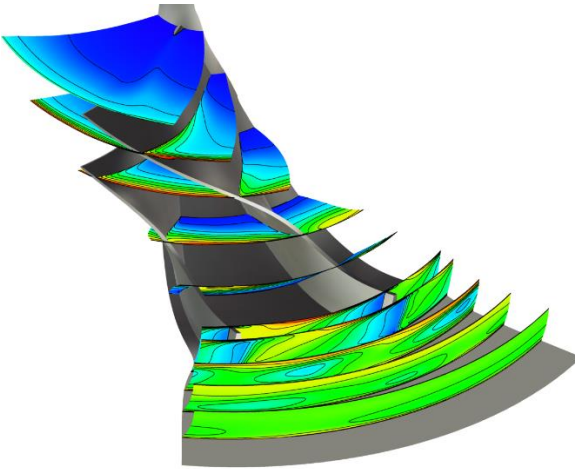


Fig. 16: Design 3: Entropy and entropy isolines along streamwise cuts

Design 1 is characterized by a lower efficiency as listed in table 2. Comparison of figures 14 and 15 shows that the entropy increases in streamwise direction over the blade and carries into the diffuser. Design 3, which shows a significantly increased efficiency exhibits significantly lower levels of entropy across the blade and in the diffuser.

The absolute radial velocity at 50% of the span height is shown in figures 17 to 19 for the original and optimal designs 1 and 3. The velocity isolines give an indication of the flow deviation at the trailing edge of the impeller. Design 3 in fig. 19 shows the flow is more aligned with the blade at the trailing edge, which results in less mixing of the flow and consequently higher efficiencies. Design 3 is indeed characterized by the highest efficiency among the retained optimized geometries. Design 1 in fig. 18 shows the highest flow deviation resulting in a lower efficiency.

While figures 11 to 13 provide an illustration of the shape deformation of the hub across the Pareto optimal designs, the differences in blade shape and location are visible in figures 17

to 19. As an example the distance between the main blade and splitter blade is significantly larger in design 3 compared to the original design, while design 1 shows a stronger sweep in the second part of the blade in streamwise direction being one reason of the lower efficiencies.

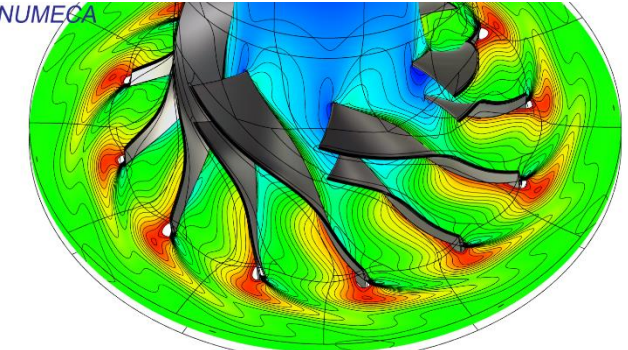


Fig. 17: Original Design: 3D geometry shape and absolute radial velocity at mid-span plane (120,000rpm near stall)

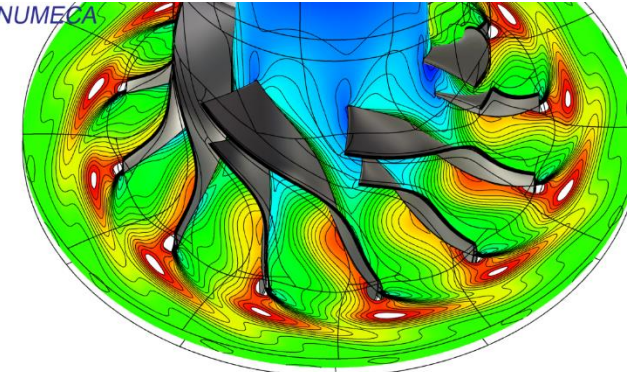


Fig. 18: Deterministic design 1: 3D geometry shape and absolute radial velocity at mid-span plane (120,000rpm near stall)

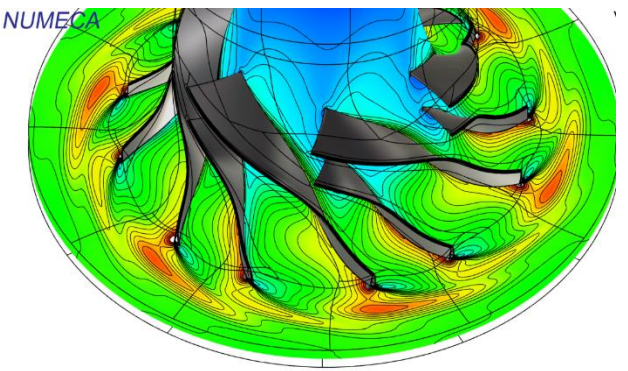


Fig. 19: Deterministic design 3: 3D geometry shape and absolute radial velocity at mid-span plane (120,000rpm near stall)

8.2. Robust design optimization

A previous study [10] showed the necessity of multipoint robust design optimization if the machine is operated outside

the design point. The robust design optimization in [10] led indeed to a design that allowed for significant reduction in the variability of the responses in the presence of uncertainties. A performance curve performed on the robust optimal designs showed that the variability in the design point – which was used for the single point robust design optimization – was reduced, but at the expense of increased variability of the responses in off-design points. A conclusion from that study was the necessity of multipoint robust design optimization as in this present work. At the same time the hypothesis arose that a deterministic multipoint optimization without explicit formulation of optimization objectives in a robust way, i.e. in form of minimizing the standard deviation of quantities of interest, could lead to globally more robust designs.

Figures 20 to 25 show several two-dimensional Pareto diagrams resulting from the robust design optimization. The quantities of interest are thus either their mean value or standard deviation. For reasons of comparability, UQ simulations were performed on the obtained deterministic optimal designs as well as on the original design. This allows to plot them in terms of their statistical moments together with the results of the robust design optimization.

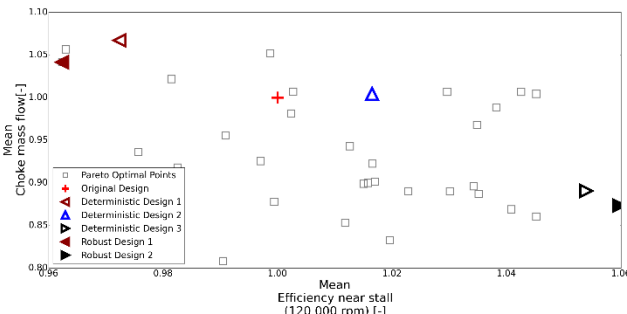


Fig. 20: Pareto plot for mean choke mass flow over mean efficiency at 120,000rpm

Figure 20 shows the mean choke mass flow over the efficiency near stall for 120,000rpm for the original design together with the two robust optimal designs selected and the three deterministic optimal design retained. It is seen that the deterministic designs lay along the Pareto frontier and are optimal in the sense of mean value of choke mass flow and efficiency near stall at 120,000rpm. Figures 21 shows the Pareto diagrams for the standard deviation of choke mass flow over the mean efficiency. Figure 22 shows the standard deviation of efficiency over the choke mass flow, where it is seen that design 1 and 3 are close to the Pareto frontier, while design 2 is not. The two robust optimal designs selected lie both along the Pareto frontier of standard deviation of choke mass flow over mean efficiency in fig. 21. The robust design 1 that shows an increase in mean choke mass flow, shows a significant reduction in standard deviation of efficiency. This was not achieved by any of the deterministic optimal designs and it can be supposed that this is a consequence of to the explicit definition of an objective to minimize the standard deviation of choke mass flow. This comes however at the expense of a decreased mean pressure ratio and increased

mechanical stresses as seen in fig. 23 to 25. The robust design 2 that increases the mean efficiency near stall even more than the deterministic design 3, shows a smaller increase in standard deviation of choke mass flow compared to the deterministic design 3, while the standard deviation in efficiency is slightly smaller for the robust design 2.

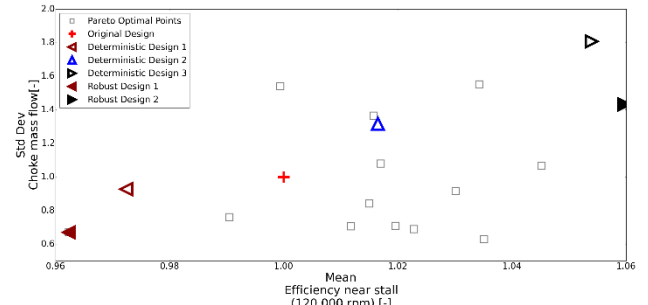


Fig. 21: Pareto plot for standard deviation choke mass flow over mean efficiency at 120,000rpm

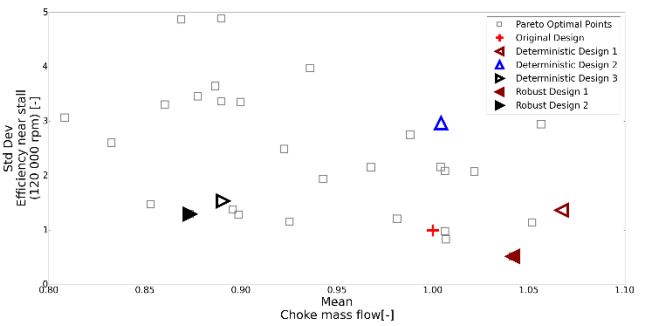


Fig. 22: Pareto plot for standard deviation efficiency over mean choke mass flow at 120,000rpm

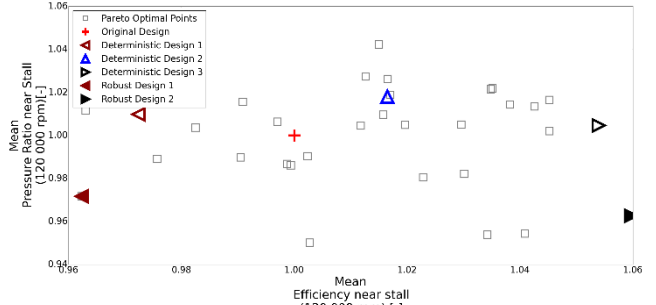


Fig. 23: Pareto plot for mean pressure ratio over mean efficiency at 120,000rpm

Table 3 summarizes the mean values used for figures 20 to 24 and table 4 the standard deviations. Comparing tables 2 and 3 it can be seen that the deterministic global values are close to the mean values. This is case specific, highly dependent on the input uncertainties, and based on the authors experience not a general conclusion.

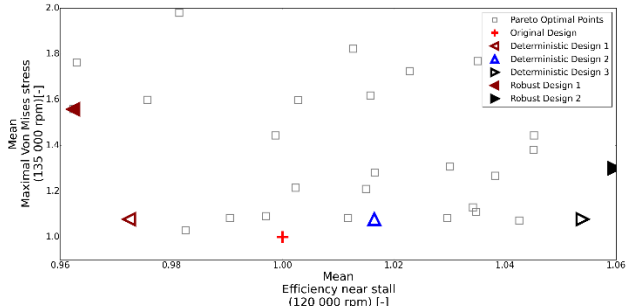


Fig. 24: Pareto plot for mean von Mises stresses mean efficiency at 120,000rpm

Table 3. Normalized mean objective function values of all optimal design.

Mean	η_{120}	η_{40}	m_{choke}	Π_{120}	Π_{40}	$\sigma_{\text{von Mises}}$
Original	1	1	1	1	1	1
Design 1	0,972	0,980	1,067	1,010	1,004	1,078
Design 2	1,016	1,014	1,004	1,018	1,001	1,045
Design 3	1,054	1,030	0,891	1,005	0,999	1,043
Robust 1	0,962	0,973	1,042	0,972	1,000	1,558
Robust 2	1,060	1,015	0,873	0,963	0,991	1,301

Table 4. Normalized standard deviation of objective function values of all optimal design.

Std. dev.	η_{120}	η_{40}	m_{choke}	Π_{120}	Π_{40}
Original	1	1	1	1	1
Design 1	1,368	0,981	0,928	1,715	1,213
Design 2	2,966	1,277	1,317	0,891	1,226
Design 3	1,538	1,281	1,808	0,601	1,443
Robust 1	0,521	0,804	0,670	---	---
Robust 2	1,298	1,151	1,433	---	---

As seen in fig. 21 the standard deviation of the choke mass flow increases for the three selected designs with a tendency of increasing standard deviation from design 1 over design 2 to design 3. It can also be seen that robust design 1 reaches a reduction in standard deviation of choke mass flow below the value of the original design and below the value of the deterministic design 1. Plotting the PDFs of the deterministic designs retained, as shown in fig. 25, all three optimal designs and the original design show narrow and symmetric PDFs. The fact that the PDFs are symmetric means that the variation of the choke mass flow over the range of the uncertainties is approximately linear.

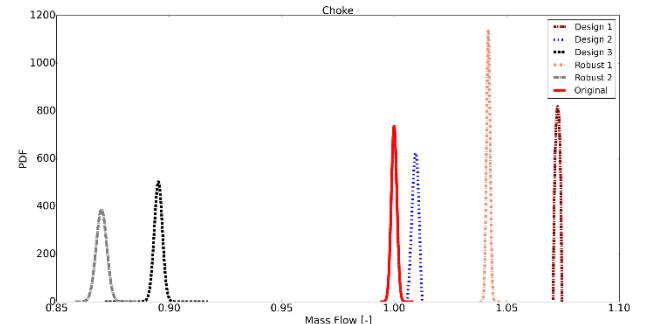


Fig. 25: Reconstructed choke mass flow PDFs for operating point near choke at 120,000rpm

Figure 22 shows a slight increase in standard deviation in efficiency for design 1 and 3 and a significant increase for design 2. Consequently the PDF shape of the isentropic efficiency are wider for the optimal designs compared to the original designs as seen in fig. 26. The robust design 1, however, clearly reduces the width of the distribution. The same applies to the pressure ratio shown in fig. 27, the robust design can narrow the spread of the response.

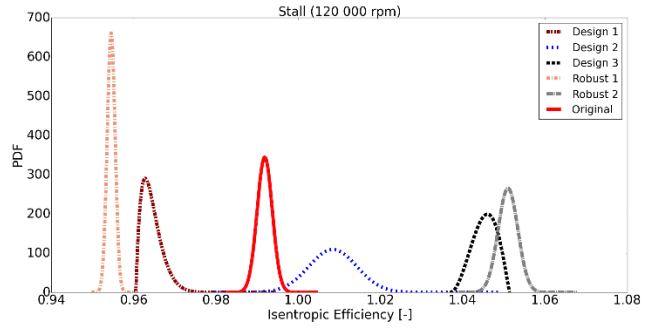


Fig. 26: Reconstructed isentropic efficiency PDFs for operating point near stall at 120,000rpm

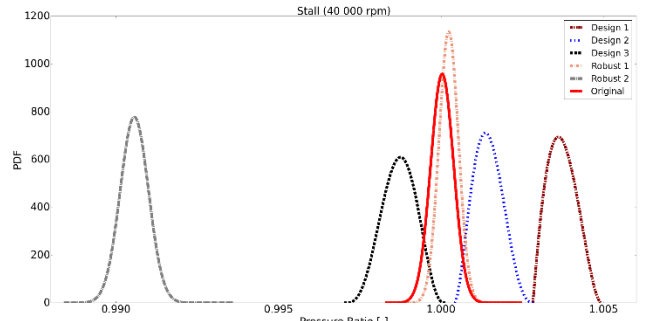


Fig. 27: Reconstructed pressure ratio PDFs for operating point near stall at 40,000rpm

An important element in understanding the behaviour of the machine is to identify the origins of the spread in output quantities, such as choke mass flow, efficiency or pressure ratio. As described in section 3.4 scaled sensitivity derivatives allow to assess the influence of the individual uncertainties on the solution.

Figure 28 shows the scaled sensitivities of the choke mass flow with respect to the three uncertainties included in this study as

defined in section 5.3. It is seen that the tip clearance shows first the largest influence on the choke mass flow and second that this influence is equivalent for the three designs retained. The diagram is to read as follows: decreasing the tip clearance leads in an increase of the choke mass flow.

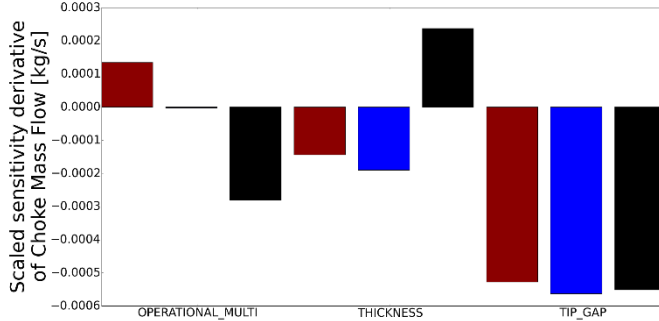


Fig. 28: Scaled sensitivities of choke mass flow for design 1 (brown), design 2 (blue), and design 3 (black)

The influence of the blade thickness distribution depends on the design, while decreasing the blade thickness distribution leads to an increase of the choke mass flow for designs 1 and 2, an increasing in the blade thickness distribution leads to an increase in choke mass flow for design 3.

Scaled sensitivity derivatives can be calculated for all computed quantities with respect to all uncertainties. Figure 29 shows the scaled sensitivity of the isentropic efficiency at 120,000rpm. Also for the efficiency the tip clearance has the highest sensitivity on the solution, in this case, and in contrast to the choke mass flow sensitivities, the sensitivity of designs 1 and 3 is significantly smaller than the sensitivity of design 2. This means that design 2 is the design most sensitive to variations in the tip clearance. Only design 3 has a notable sensitivity of the efficiency to the blade thickness distribution, while designs 1 and 2 are basically insensitive to the blade thickness distribution.

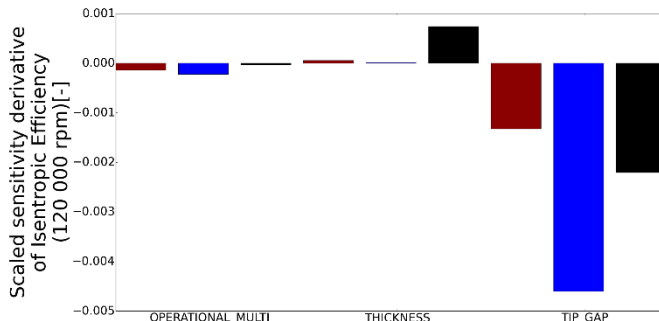


Fig. 29: Scaled sensitivities of isentropic efficiency at 120,000rpm for design 1 (brown), design 2 (blue), and design 3 (black)

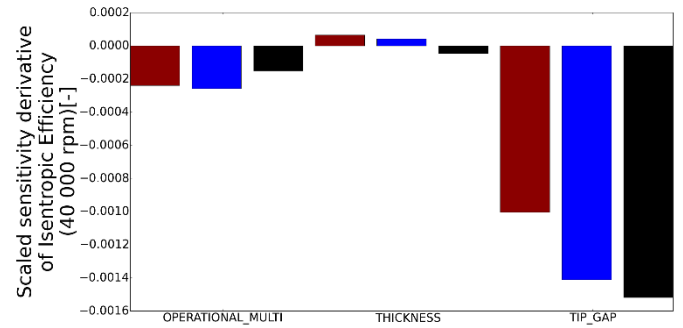


Fig. 30: Scaled sensitivities of isentropic efficiency at 40,000rpm for design 1 (brown), design 2 (blue), and design 3 (black)

Comparison of fig. 29 with fig. 30 shows that the influence of uncertainties varies also with the operating conditions as shown on the example of the efficiency at 120,000rpm and 40,000rpm respectively. While the tip clearance has by far the most important influence on the efficiency at 120,000rpm on design 2, the differences are much less pronounced at 40,000rpm. Design 3 is even the most sensitive to the tip clearance at 40,000rpm. It must be noted, however, that the scaled sensitivity, which has the unit of the quantity itself is shown in absolute values. In absolute values the sensitivity of design 2 decreases by a factor of nearly 3 passing from 120,000rpm to 40,000rpm, while the sensitivity of design 3 decreases by approximately 25%.

Scaled sensitivities of the two retained robust designs are shown in fig. 31, fig 34 and fig. 35. As seen from fig. 20, the robust design 1 is comparable to the deterministic design 1 and the robust design 2 is comparable to the robust design 3, which is also reflected in the colour code of the following figures. With respect to the choke mass flow dependency on the tip clearance, it can however be noted that in contrast to the deterministic designs 1 and 3, the scaled sensitivity derivatives of the robust designs vary by a factor 4, while the deterministic designs have comparable sensitivities. The sensitivity on the blade thickness of the two robust designs is comparable as seen in fig. 31, while it changes sign for the deterministic designs 1 and 3 as seen in fig. 28.

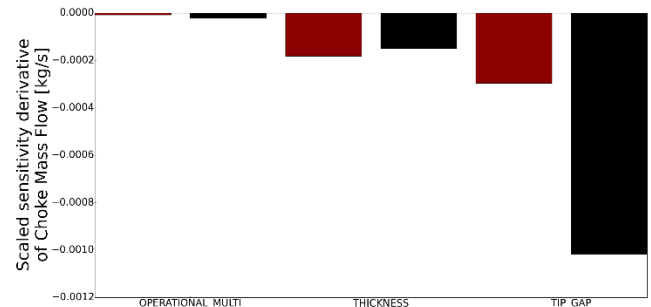


Fig. 31: Scaled sensitivities of choke mass flow for robust design 1 (brown) and robust design 2 (black)

The scaled sensitivity of the isentropic efficiency at 120,000rpm with respect to the tip clearance also changes sign

for the two retained robust designs (fig. 34), while deterministic designs 1 and 3 did not show a dependency with opposite signs. Increasing the tip clearance increases the efficiency of robust design 1, while increasing the tip clearance decreases the efficiency of robust design 2. This behaviour of robust design 1 is counter intuitive and the change in sign is not observed at 40,000rpm. Figures 15 and 16 compare the entropy at several streamwise cuts between design 1 and 3, where design 3 shows lower entropy levels and higher efficiencies. The blade shape of design 1 is less appropriate in terms of efficiency as discussed above. To explain the positive sensitivity of the efficiency with respect to the tip gap of design 1, figures 32 and 33 show the entropy for the lowest and highest tip gap value of design 1. It is seen that a larger tip gap leads, due to the specificities of this particular blade design, to lower entropy levels and thus higher efficiencies.

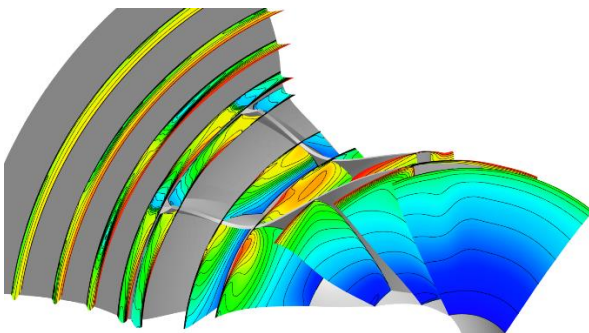


Fig. 32: Entropy for design 1 near stall at 120,000rpm with minimum tip gap.

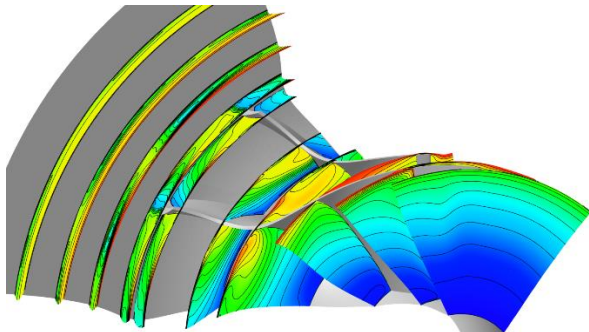


Fig. 33: Entropy for design 1 near stall at 120,000rpm with maximum tip gap.

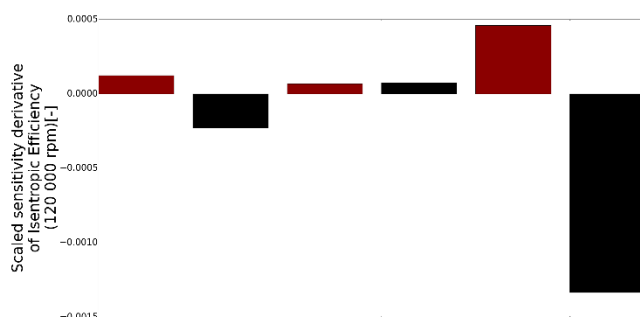


Fig. 34: Scaled sensitivities of isentropic efficiency at 120,000rpm for robust design 1 (brown) and robust design 2 (black)

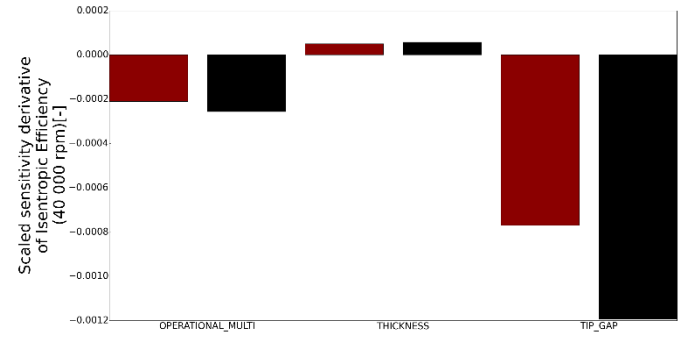


Fig. 35: Scaled sensitivities of isentropic efficiency at 40,000rpm for robust design 1 (brown) and robust design 2 (black)

Cartesian plots along sections in the flow field allow extracting ranges of variability of output quantities. Figures 36 to 38 show Cartesian plots of the pitchwise averaged total temperature and pressure along spanwise sections at the leading and trailing edge of the main blade respectively. Figure 36 shows the pitchwise averaged total temperature over span. At the leading edge (LE) the variability is small and the difference in mean value between the different designs is small, while the differences in mean value at the trailing edge (TE) are more pronounced. The variability increases with increasing span and reaches its maximum (largest standard deviation visualized by the bars) close to the tip. Given that the uncertainty on the tip gap was shown to have the most important influence on the flow performance this is explained by different flow conditions close to the tip of the blade.

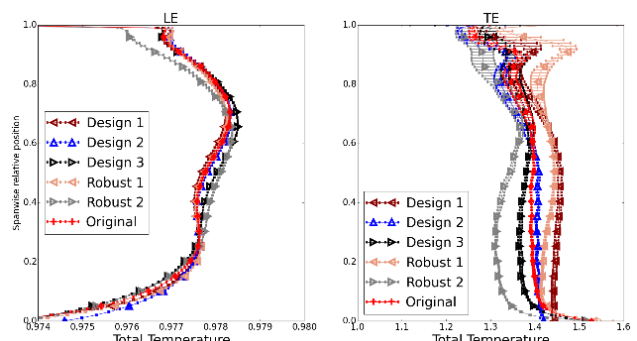


Fig. 36: Total temperature at near choke point (120,000rpm)

Figures 37 shows the pitchwise averaged total temperature over span for the operating point close to stall at 40,000rpm. The total temperature distribution is significantly different at the leading edge for the different designs. The mean value of the total temperature reduces for designs 1 and 2 and increases for design 3, while their variability is almost constant across the various designs. At the trailing edge the variability in pitchwise averaged total temperature is smaller for all designs at low span positions, while it also increases with increasing span. It can be noted that the original design and design 2 show very similar mean values and variability, while design 1 and 3 are offset, but with the same trend. Design 2 is the design that lies closest to the original design on the various global quantity Pareto plots. Figure 38 shows the pitchwise averaged total

temperature over span for the operating point close to stall at 120,000rpm. It must be noted that design 1 has a significantly different variability compared with the other designs at the leading edge. In particular, the standard deviation is significantly higher at midspan positions, while the mean value is similar. Figures 45 and 46 show the colour contours that explain this high standard deviation, which is a result of the uncertainty in the tip clearance. The influence of a robust design optimization formulation becomes visible if the distribution of the robust design 1 is compared with the one of the deterministic design 1. Both designs lie in the same region of the performance Pareto plots, but the robust design limits largely the variation of total temperature distribution of span, as seen in fig. 38.

At the trailing edge the variability is larger for all designs at low span positions and close to the tip of the blade. Most notably the original design exhibits a relative high variability at low span position in comparison with the optimal designs, which are as a consequence more robust with respect to the pitchwise averaged total temperature over span (fig. 38).

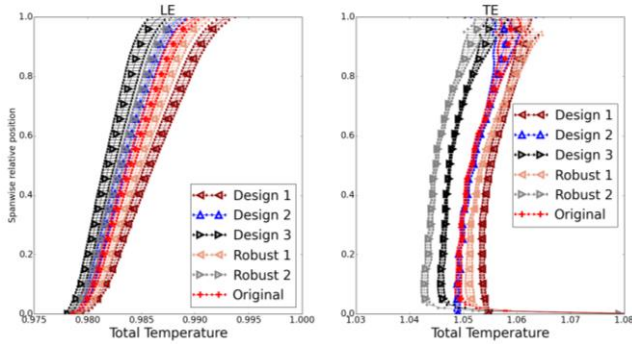


Fig. 37: Total temperature at near stall (40,000rpm)

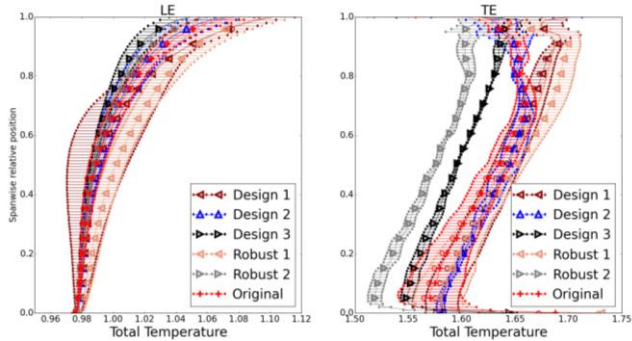


Fig. 38: Total temperature at near stall (120,000rpm)

Figure 39 shows the total pressure at the operating point near stall at 40,000rpm. It shows a very fundamental property of non-deterministic simulations. At the leading edge the mean value of the pitchwise averaged total pressure is notably different from the deterministic total pressure value obtained at the nominal conditions of the input uncertainty distributions (circles in fig. 39). This means that running the deterministic simulation with its nominal conditions gives the values

indicated by the circles as response, while the mean value calculated if the uncertainties around these nominal conditions are taken into account are given by the other symbols. Their range of variability is again visualized by the bars. In general, if a given output quantity (here the pitchwise averaged total pressure) shows a non-linear behaviour the range of variability of the input uncertainties, the mean value of the output quantity is different from the deterministic value at its nominal conditions.

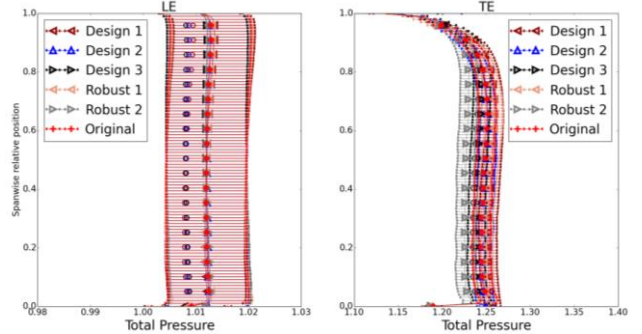


Fig. 39: Total pressure at near stall (40,000rpm)

The above figures 36 to 39, show the spanwise variability of pitchwise averaged quantities. Colour contours can be used to show the origins of these variabilities if for example the colour contour of the absolute total temperature is plotted for the minimum and maximum tip gap configuration that are part of the UQ simulations. Figure 40 to 43 show the absolute total temperature on planes that are constant in spanwise direction; fig. 41 and fig. 42 for a spanwise value of 0.1 and thus close to the hub and fig. 43 and fig. 44 for a spanwise value of 0.96 close to the tip. The tip gap is chosen as it was identified as the most influential uncertainty. The near stall operating point at 120,000rpm is retained for this comparison at the example of design 1.

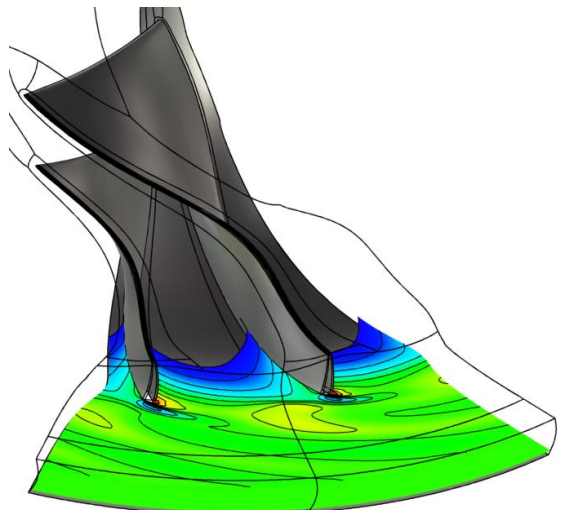


Fig. 41: Absolute total temperature for operating point near stall at 120,000rpm for design 1 and minimum value of tip gap uncertainty at spanwise position 0.1

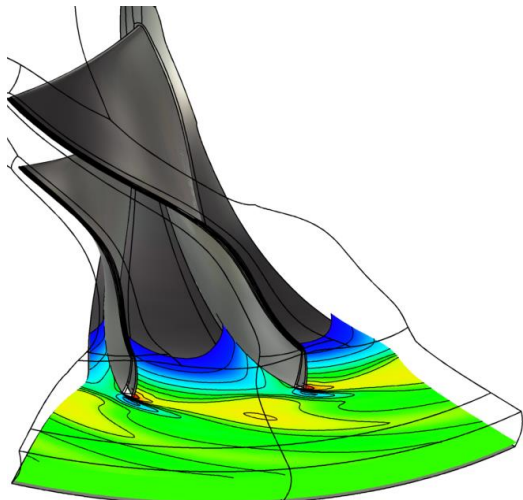


Fig. 42: Absolute total temperature for operating point near stall at 120,000rpm for design 1 and maximum value of tip gap uncertainty at spanwise position 0.1

Comparing fig. 41 and fig. 42 it is seen that the colour contours vary notably close to the trailing edge for a spanwise position of 0.1. If compared with fig. 38 it is seen that this is the area where design 1 shows a large standard deviation. Figures 43 and 44 show the minimum and maximum configuration at a spanwise position of 0.96. The difference close to the trailing edge leads also here to notable variations. It is interesting to note that the colour contours show significantly different responses in the middle of the blade (in streamwise direction) as seen in fig. 43 and 44. Figure 38 shows a large variation at midspan close to the leading edge. This variation seems to be reduced in streamwise position. Finally, fig. 45 and fig. 46 show the absolute total temperature close to the leading edge at mid-span position. These differences in magnitude are responsible for large variability at mid-span close to the leading edge.

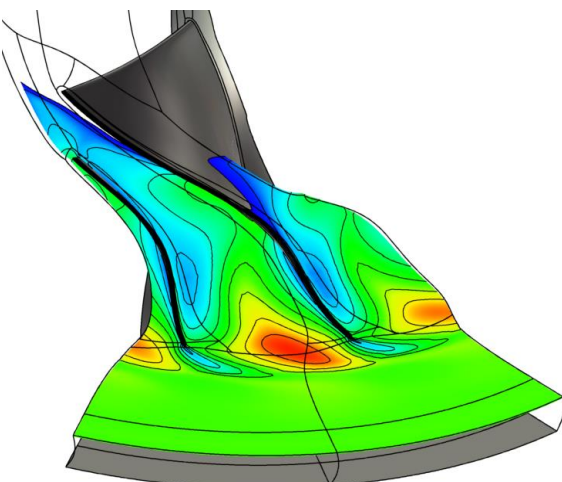


Fig. 43: Absolute total temperature for operating point near stall at 120,000rpm for design 1 and minimum value of tip gap uncertainty at spanwise position 0.96

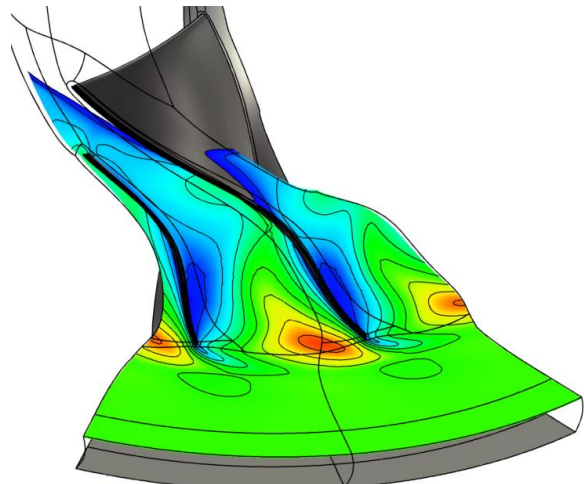


Fig. 44: Absolute total temperature for operating point near stall at 120,000rpm for design 1 and maximum value of tip gap uncertainty at spanwise position 0.96

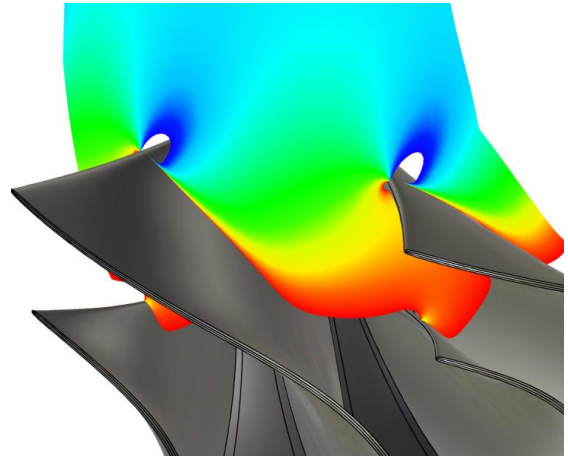


Fig. 45: Absolute total temperature for operating point near stall at 120,000rpm for design 1 and minimum value of tip gap uncertainty at mid-span position

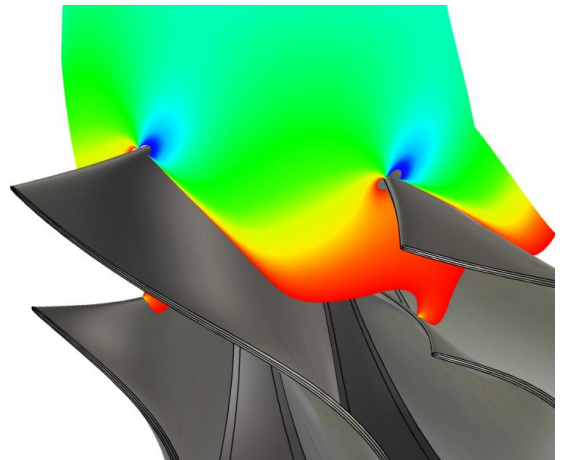


Fig. 46: Absolute total temperature for operating point near stall at 120,000rpm for design 1 and maximum value of tip gap uncertainty at mid-span position

9 Conclusions

A recently developed strategy for Robust Design Optimization (RDO), i.e. optimization under uncertainties while reducing the variability of the system output with respect to the input uncertainties is applied to a turbocharger impeller. A recent application of this RDO strategy to an axial compressor blade showed that a multi-point formulation is of foremost importance for an industrial application of robust design optimization, since otherwise off-design points become less robust. Given that the investigated turbocharger compressor has an active self-recirculation casing treatment design, the multi-point optimization problem combines three operating points on two different speed lines. Both fluid and structural simulations are performed and mechanical stresses are included as constraints in the optimization problems.

Two design optimization studies are performed, first a deterministic multipoint optimization and second, a robust multipoint design optimization accounting for uncertainties in the optimization process. The robust design optimization includes explicit definition of objective functions on the mean value and standard deviation of output quantities. It is shown that the multipoint formulation of the deterministic optimization leads to designs which lie on or close to the robust Pareto fronts. It was supposed before the study that a multipoint formulation might lead to somewhat more robust designs compared with a single point optimization of the same configuration, the clarity of the present findings is nevertheless unexpected.

The objectives increasing choke mass flow and increasing efficiency are strongly conflicting and a clear Pareto front is formed. The further mechanical stress levels tend to increase with higher efficiencies. The original design is located very close the Pareto front and provides already a good compromise of all conflicting objectives, but designs can be found that increase both mean values of choke mass flow and efficiency by approximately 1.5% for each. In addition the robust design formulation shows the capability of reducing the standard deviations of output quantities below levels reached by the deterministic design optimizations and thus allows to find more robust designs in terms of these objectives.

The UQ post-processing tools are used to analyze and discuss the different designs showing how scaled sensitivities can precisely identify the uncertainties responsible for variability in the response.

10 References

- [1] Demeulenaere A, Bonaccorsi JC, Gutzwiller D, Hu L, Sun H, 2015, Multi-disciplinary multi-point optimization of a turbocharger compressor wheel, Proceedings of the ASME GT 2015, GT2015-43631
- [2] Golub GH, Welsch JH, 1969, Calculation of Gaussian Quad-rature rules, *Math. Comp.* 23:221-230
- [3] Hirsch C, Buggeda G, Szumbarski J, Laniewski-Wolk L, Pons-Prats J, Wunsch D, 2017, UMRIDA: Uncertainty Management for Robust Industrial Design, Chapter IV.1
- [4] Hu L, Sun H, Yi J, Curtis E, Zhang J, Yang C, Krivitzky E, 2013, Numerical and experimental investigation of a compressor with active self-recirculation casing treatment for a wide operating range, *Proceeding of the Inst. of Mech. Eng., Part D: Journal of Automobile Engineering* 2013 227-1227
- [5] Loeven, GJA, Witteveen JAS, Bijl H, 2007, Probabilistic collocation: an efficient non-intrusive approach for arbitrarily distributed parametric uncertainties, *Proc. 45th AIAA Aerospace Sciences Meeting and Exhibit*, AIAA paper 2007-317, Reno, United States
- [6] Mathelin L, Hussaini MY, 2003, A stochastic collocation algorithm for uncertainty analysis, Technical Report NASA-CR-2003-212153, NASA Langley Research Center
- [7] Pearson K, 1895, 1901, 1915, *Philosophical Transactions of the royal Society of London*. 8 laws variant
- [8] Smolyak S, 1963, Quadrature and Interpolation formulas for tensor products of certain classes of functions, *Dokl. Adad. Nauk USSR B*, 240-243
- [9] Turgeon E, Pelletier D, Borggaard J, 2003, Applications of continuous sensitivity equations to flows with temperature-dependent properties, *Numerical Heat Transfer*, **44**, 611-624
- [10] Wunsch D, Nigro R, Coussement G, Hirsch C., 2015, Quantification of combined operational and geometrical uncertainties in turbomachinery design, *Proceedings of the ASME GT 2015*, GT2015-43399